Article:

Holladay, P., Burstow, M., Franklin, F. et al. (2026) Peridynamic-inspired bonds to address strain incompatibility in modelling rail damage through ratchetting strain accumulation. Wear, 602. 206900. ISSN: 0043-1648

https://doi.org/10.1016/j.wear.2026.206900

Peridynamic-inspired bonds to address strain incompatibility in modelling rail damage through ratchetting strain accumulation.

Philomenah Holladay[a,*], Mark Burstow[b], Francis Franklin[c], Adam Wilby[d], David I Fletcher[a]

[a] *School of Mechanical Aerospace and Civil Engineering, University of Sheffield, Mappin Street, Sheffield, S1 3JD, UK*
[b] *Network Rail Infrastructure Ltd, The Quadrant, Elder Gate, Milton Keynes, MK9 1EN, UK*
[c] *University of Newcastle upon Tyne, Stephenson Building, Newcastle upon Tyne, NE1 7RU, UK*
[d] *British Steel, Brigg Road, Scunthorpe, Lincolnshire, DN16 1XA, UK*

Abstract

Incremental accumulation of strain by rail steels in response to repeated compressive shear loading above the shakedown limit determines rail maintenance requirements and is a precursor to the initiation of defects that may develop into safety critical cracks and broken rails. Most modelling techniques struggle, through limitations in scale or on computational expense, to evaluate the long-term performance of rail steels, addressing this by simplifying the rail material response, considering only the ratchetting response and defining failure by a critical value of accumulated strain. However, these simplified models of ratchetting response are unable to capture experimentally observed wear behaviour of rail steels prior to strain exhaustion. Here we demonstrate validation across a range of contact pressures characteristic of rail operation that this behaviour can be represented through introduction of peridynamic-inspired bonds to quantify strain partitioning and resultant failure in the material. This is a crucial step in linking microstructural and metallurgical scale behaviour to macro level wear and damage development for maintenance planning. The newly modelled failure mechanism domi-

*Corresponding Author
Email address: pholladay1@sheffield.ac.uk (Philomenah Holladay)

nates at lower numbers of contact cycles (<10,000) and under lower strain that acts prior to strain exhaustion and was previously neglected. Through capturing strain partitioning with peridynamic-inspired bonds, inconsistencies between wear experiments and predicted wear rates considering strain exhaustion alone can be addressed. Parameters defining the additional wear mechanism are explored here to understand how they represent the physical failure process, and how they can be combined with existing understanding of material failure through strain exhaustion.

Keywords: Wear Modelling, Peridynamics, Ratchetting, Strain Incompatibility, Rail Steel

---

1. Introduction

This paper develops and validates a new approach to quantify early stage wear prior to ductility exhaustion, within the context of a ratchetting strain accumulation damage model, addressing a previously neglected strain incompatibility between adjacent regions of microstructure with differing properties subject to identical loading. The accumulation of plastic strain by rail steels in response to large compressive shear stresses, produced by the normal compressive loads and tangential traction (shear) that arise during wheel rail contact, will vary depending on the steel grade, i.e. its metallurgical composition and heat treatment [1]. Repeated rolling-sliding contact above the shakedown limit will cause ductile materials, including rail steels, to incrementally accumulate strain [2]. This accumulation of strain and accompanying microstructural deformation is a good indicator of the point of initiation and later propagation of cracks that could develop into safety critical defects which could lead to complete failure of the rail. As ductility is exhausted, cracks initiate and propagate in the deformed and heavily strained material, resulting in delamination wear or the development of more severe rolling contact fatigue (RCF) cracks [3, 4, 5, 6]. Both require intervention on the part of rail infrastructure managers through costly maintenance such as re-profiling, grinding, welding, and in some cases complete renewal of the rail. Network Rail spent £2,282 million on maintaining its network in Great Britain between April 2023 and March 2024, including maintenance activities such as those described above [7]. Therefore, prediction and prevention of rail defects that form as a result of unrestricted plastic deformation is a priority. Rail Safety and Standards Board-sponsored research in Great Britain led to the development of frictional energy models used to predict locations of potential damage due to the contact forces [8]. Network Rail uses this model to impose a variable usage charge on train operators to recover some of the maintenance and renewal costs associated with correcting the rail damage as a result of wear and RCF [9]. The variable use charge has influenced vehicle design to be less damaging to both the rail and the wheel, and the introduction of harder, more wear resistant, premium grade rail steels has been shown to slow the geometric deterioration that can cause the contact conditions to change detrimentally [10, 11, 12]. However, the response of different rail steel grades to the complex and variable contact conditions experienced in service remains difficult to predict [13].

Modelling the response of steel to applied loads offers insight into the dependence of the behaviour outlined above on rail steel compositions. Several different methods have been applied to the problem. The technique which has been widely applied to modelling rail steel deformation and failure since the 1990s is Finite Element Analysis (FEA), used to model the ratchetting response [14, 15, 16], deformation [17], and damage development [18, 19, 20].However, due to limitations in computational power, for plasticity modelling most FEA is only able to simulate the first few hundred loading cycles a rail might experience. This restricts the effectiveness of the technique when evaluating the long-term performance of rail steel grades which will experience millions of loading cycles during service. Therefore, alternative modelling methods have seen increasing application to the problem of rail failure.

Molecular dynamics is another modelling technique which has seen increasing interest within the field of contact mechanics, with it being previously employed to investigate asperity contact [21], and ratchetting behaviour [22], on an atomic scale. However, when applied to the problem of predicting rail failure [23], the complex atomic structure of a common rail steel constituent, pearlite, made up of lamellar of body centred cubic ferrite (Fe) and orthorhombic cementite (Fe3C) is omitted in favour of a simplified purely body centred cubic structure [23]. This can be attributed to the difficulty in interpreting the behaviour of orthorhombic structures in molecular dynamics post processing algorithms. The structure of these components is important when attempting to predict crack initiation as, fundamentally, plastic deformation and void formation which lead to crack initiation originating in the movement of dislocations through the atomic lattice of these structures [4], [24]. Furthermore, due to the atomic scale of molecular dynamic simulations, modelling a volume that is representative of macro-scale rail behaviour is restricted by its computational expense. To avoid such difficulties, more macro-scale techniques are often preferred.

Peridynamics is a more recently developed modelling technique which has been utilised in problems of rail failure [25], [26]. The technique is an extension of continuum mechanics that allows for the modelling of discontinuities within a material. A body is discretised into nodes, which interact with other nodes within a region of influence through bonds. The bonds represent a summation of the interatomic and hydrostatic forces that resist void formation and crack growth in a material [27]. When the body is deformed, the bonds stretch as the nodes move relative to one another. If the stretch exceeds a given value, defined to align with the material's fracture toughness, energy density, or fatigue life, the bond will fail, representing the formation of voids or cracks in the material between two nodes [28, 29, 30]. A sliding point contact and the resulting crack initiation and growth have been previously modelled using Peridynamics [31]. Although the model succeeds in predicting the formation of micro-cracks, its applications have not yet focused on the removal of the material through wear or subsequent material damage. Much like finite element models, peridynamic equations are computationally expensive and the mesh refinement methods employed mean that only the area directly below the point contact can be accurately modelled, limiting the size of peridynamic simulations [32]. Additionally, small time-steps, micro and nano seconds, are required to achieve convergence in larger models, again restricting the simulations to a small number of wheel contact cycles.

There is, therefore, an opportunity for models that employ techniques that are not restricted by computational expense. The dynamic ratchetting (Dynarat) modelling technique sought to address the limitations of computational expense experienced by other modelling techniques by utilising a hybrid approach. It combines calculated applied stresses with experimentally determined material plastic deformation response, thereby enabling simulation of a much greater number of contact cycles within reasonable timescales [33]. The model discretises a section of rail into a grid of elements called 'bricks', each of which are characterised by material properties such as shear yield and critical shear strain. This is not a finite element approach although the discretisation of the rail does have superficial similarity. Bricks accumulate strain through a ratchetting process with varying rates according to the maximum orthogonal shear stress they experience, and the work hardening behaviour of the material, defined by a modified Voce equation fitted to experimental data on strain accumulation under representative highly compressive repeated rolling-sliding contact conditions [1]. This material data effectively replaces material models that conventional finite element models would use. In versions of this model previously implemented a brick is considered to have failed once the limit of critical shear strain is exceeded, which represents ductility exhaustion, a pre-cursor to the formation of voids or cracks in the material. In recent work considering normal grade pearlitic rail steel R260, it was found that the brick model, whilst successful in representing steady state wear, faced difficulties with certain experimental behaviour, such as wear in the first few thousand contact cycles. During these early contact stress cycles, it was predicted that the critical failure strain of this harder steel had not yet been reached [34], but the presence of wear in twin disc experiments indicates an alternative failure mechanism is active at the rail steel surface. This is despite the inclusion of multi-Hertzian roughness in the maximum orthogonal shear stress calculation, meaning that near surface bricks at the rail surface experience large shear stresses characteristic of real surfaces, reaching failure strain more rapidly than if just considering smooth surface stresses.

The focus on ratchetting and ductility exhaustion in the Dynarat model leads to good predictions for the steady state material loss at high numbers of contact cycles, potentially including the severe wear regime. However, quantifying wear observed experimentally at low numbers of contact cycles and prior to ductility exhaustion, for example in the mild wear regime, requires modelling a new failure mechanism. Figure 1 shows the simulated and experimental wear rates produced under the three different contact pressures [1, 34]. The simulated wear rates are determined here using the ductility exhaustion failure mechanism alone, such that bricks are removed once they have reached a critical value of strain. At contact pressures of 1500MPa and 1200MPa, the simulated wear rates show good correlation with experimental behaviour. However, at 900MPa, the initiation of wear in the simulated response is delayed until after 10,000 cycles. The reliance on strain exhaustion alone means that wear cannot initiate in the model until the surface bricks have reached the critical value of strain. In the 900MPa case, where the maximum orthogonal shear stress, and resultant strain increment for each brick is lower than for higher contact pressures, this will not occur until after 10,000 cycles in the simulations. This, as illustrated in Figure 1, is not representative of experimental behaviour, where material removal is already underway at 10,000 cycles. This deviation between experimental and simulated response suggests that the wear mechanism is not entirely dependent on ductility exhaustion, and that the early stages of the experimentally observed wear can be in the mild wear regime before transitioning to a higher rate in the steady state. Therefore, an additional failure mechanism is required in the model to more accurately represent the initial wear behaviour.

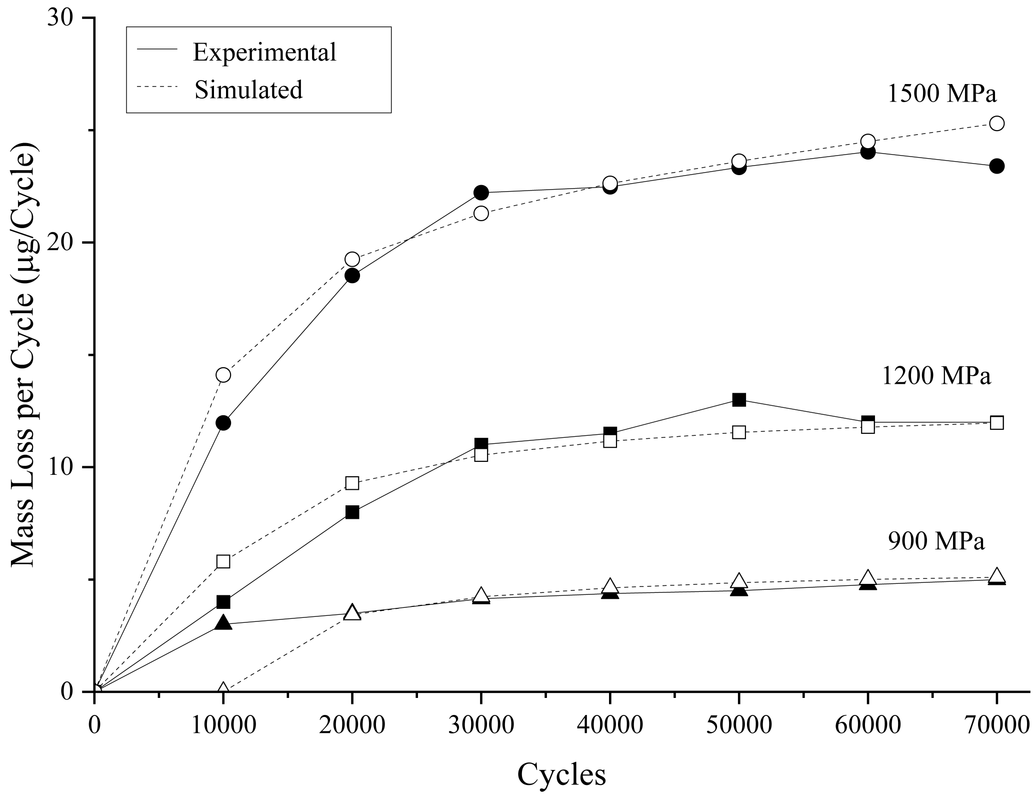

Figure 1: Simulated wear rates of R260 rail steel compared with experimentally determined wear rates under repeated rolling sliding contact, using only a strain exhaustion brick removal mechanism

An aspect of strain accumulation that was neglected in previous implementations of the Dynarat model was strain incompatibility between adjacent bricks of the material, as illustrated in Figure 2. Incompatibility may exist, for example, because microstructures are non-homogeneous and have regions with differing yield or hardening properties. Variation in the strength of the material, as a result of the differing properties of the microstructural constituents, promotes differing strain developing in adjacent regions (or bricks).

However, the surrounding material will resist this and residual stresses will develop to maintain strain compatibility during initial deformation. But just as strain accumulation has a ductility exhaustion limit, so there is a limit to the residual stress that can develop before failure as residual stress becomes insufficient to avoid adjacent regions of different mechanical properties developing incompatible strain (i.e. separating) in response to the same loading. This has been described, for example, in the case of strain partitioning (preferential straining) developing between pearlite and pro-eutectoid ferrite leading to crack initiation [35, 36].

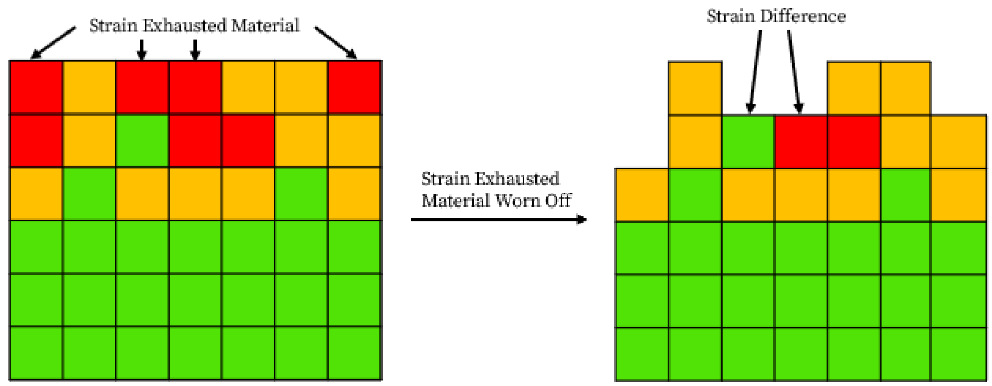

Figure 2: Schematic of strain incompatibility between adjacent material bricks

To explore the issue of strain incompatibilities between bricks this paper presents a significant advancement in ratchetting based models for rail failure. Whilst based on the semi-empirical approach of the Dynarat technique, this model also makes use of a GPU (Graphics Processing Unit) accelerated agent-based modelling environment to significantly accelerate the simulations [37]. The agent-based technique facilitates communication between material bricks about their respective strain states and the introduction of peridynamic-inspired bonds. The bonds address the wear rate discrepancy between the simulated and experimental behaviour, with the 'bonded' brick model borrowing the concept of bonded material from Peridynamic theory. As previously, the material is discretised into bricks, but the bricks are now connected by bonds, which can fail if strain compatibility criteria are exceeded. This novel failure mechanism never previously included in ratchetting simulations accounts for the strain incompatibility that can form between bricks and enables representation of the mild wear regime that ductility exhaustion alone cannot simulate. In addition to bond failure between individual bricks, the concept of bonds allows a novel representation of how regions of bricks interact to define when a brick is removed as wear debris. In combination, capturing these additional mechanisms enables the model to describe the early wear behaviour of rail steels under repeated rolling/sliding contact. To explore and validate how these bonds behave, and their effect on the ability of the model to represent experimental observations, this paper investigates the effect of different bond criteria on the wear rates of a simulated section of R260 rail steel.

2. Bonded Brick Model for Rail Failure

To make use of recent developments in computer hardware, particularly the emergence of Graphics Processing Units (GPUs) for parallel processing, the model uses an agent-based simulation written within the FLAME GPU framework (Flexible Large-scale Agent Modelling Environment for Graphics Processing Units) [37]. Prior to the introduction of bonds to define early-stage mild wear behaviour, the performance of the model in this new computing framework was explored, including cross-validation against historical data and is the subject of a separate publication [38]. Using a GPU based framework to execute the calculation required for all material elements in parallel instead of the traditional CPU code has been shown to accelerate computing time by 8 to 30 times depending on the hardware combinations considered. The computation speed increase achieved, and advantages to using the FLAMEGPU modelling framework for modelling long term material strain accumulation behaviour, can be demonstrated by comparing the time required for the Hertzian stress calculations to be computed. The calculation of the maximum orthogonal shear stresses induced from a rough surface contact has been demonstrated to benefit from a computation time that is 8.3 times faster when performed on the GPU (GeForce RTX 4070) as opposed to the CPU (Intel i5-12400) [38]. The ratchetting behaviour of the model remains largely unchanged from the original Dynarat model (Figure 3), which is summarised below but also in Refs [33, 39, 40]. Experimental data on strain accumulation, gathered through repeated highly compressive rolling-sliding contact twin disc tests, is used to represent the material behaviour. The plastic shear strain increment accumulated by each brick, each cycle, $\Delta\gamma^{ijk}$, is determined using Equation 1, where γ^{ijk} is the strain at the brick in location ijk.

$$\Delta\gamma^{ijk} = C\left(\frac{|\tau^{jk}_{zx(max)}|}{k^{ijk}_{\text{eff}}} - 1\right) \tag{1}$$

Here $\tau^{jk}_{zx(max)}$ is the maximum orthogonal shear stress at depth j and lateral position k, k^{ijk}_{eff} is the effective shear yield strength of the brick at position i,j,k in a 3D simulation, and C is the ratchetting load to ratchetting strain conversion factor which is a dimensionless stress independent constant determined experimentally from twin disc testing [41, 34]. To enable comparison with twin disc wear rates we are considering here a line contact configuration for which the peak absolute shear stress experienced during the passage of the contact varies in the j direction only, while the material extends in all three dimensions. Alternative approaches with a fully three-dimensional stress distribution, or a semi-Hertzian 'strip' based contact model [42] can also be implemented. The work hardening of the material as the simulation progresses is represented by Equation 2, using material constants m, n and p which are also determined experimentally through nano-indentation and optical microscopy of the near surface, highly deformed region of the rail steels generated during twin disc testing [1].The full procedure is the subject of a separate publication [34, 1].

$$k^{ijk}_{\text{eff}} = m\left(1 - e^{-n\gamma^{ijk}}\right)^{p} \tag{2}$$

The material constants, including the work hardening parameters, initial shear yield stress, and critical strain at failure vary between bricks and are distributed statistically, assuming a normal distribution of properties across all the bricks in a simulation. They may also be distributed to represent a real microstructure [43, 44]. The total accumulated plastic shear strain for brick ijk, γ^{ijk}, will increase each cycle (t) according to Equation 3.

$$\gamma^{ijk}_{t+1} = \gamma^{ijk}_{t} + \Delta\gamma^{ijk} \qquad \text{where } |\tau^{jk}_{zx(max)}| > k^{ijk}_{\text{eff}} \tag{3}$$

If the applied shear stress is greater than the shakedown limit, including the effect of strain hardening, this will continue until a critical value of shear strain is reached. At this point the brick has reached ductility exhaustion and is considered failed material. If the applied stress in a contact passage is below the shakedown limit there is no increment of plastic strain.

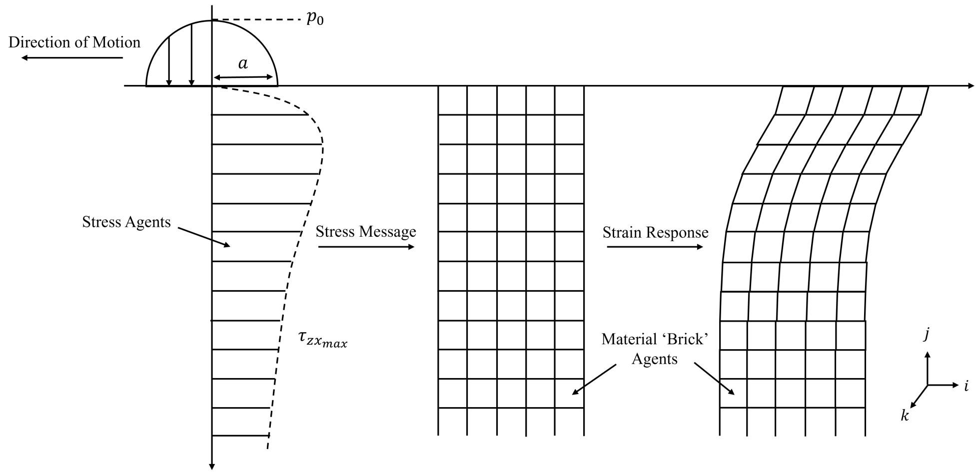

Figure 3: ratchetting behaviour of Bonded-Brick Model in Agent Based Modelling Software FLAMEGPU [37]

2.1. Strain incompatibility and removal of worn material

In previous applications of the Dynarat technique, material could be removed as wear debris if it has reached ductility exhaustion, is located at the contact surface, and unsupported by surrounding material. Alternatively, if material failed below the surface, it was taken to lose its ability to support tensile or shear loads, indicating development of microcracks [44]. The wear behaviour relied on an elaborate mechanism of brick removal dependent on the condition (failed or healthy) of neighbourhoods of bricks [33]. Integrating the new peridynamic-inspired bond failure mechanism enables reconsideration of these wear and crack initiation criteria to better represent experimentally observed material degradation focusing on strain incompatibility between neighbouring locations in the model. Nanometre resolution digital image correlation of microstructural deformation using scanning electron microscopy applied to ferritic pearlitic steel, with comparable features to that of a conventional rail steel, identified that localised strain accumulation in ferrite phase leads to damage initiation that could lead to macro-scale fracture [36]. The damage takes the form of de-cohesion between the ferrite and pearlite phases which leads to initiation of voids and cracks. The scale of such a de-cohesion event is comparable to brick size in the Dynarat model (between 1-10μm). The strain-difference failure mechanism is intended to represent the experimentally observed de-cohesion between material elements as a result of the preferential accumulation of strain which could lead to material removal from the surface and crack initiation subsurface

As strain accumulates in each brick it can be identified where strain incompatibility develops between a brick and its neighbours. This has facilitated the introduction of the new failure mechanism using peridynamic-inspired bonds. The bonds represent the residual stresses that accumulate in material as it resists the development of a strain incompatibility, much like traditional peridynamic bonds, they incorporate the sum of interatomic forces that prevent void and dislocation formation in materials. However, the peridynamic equations of motion do not naturally lend themselves to the Dynarat model. Which uses the previously described hybrid calculation, alongside experimentally derived material property data representing plastic ratchetting response to achieve a high number of cycles in a short amount of computation time. Furthermore, the displacement, or strain, at each node (brick) has already been calculated by the ratchetting equations, such that the peridynamic equations of motion are not required. Instead, the model adopts the principle of bonds between material elements that can be broken if certain conditions, described below, are met, and incorporates the established Dynarat ratchetting equations instead of the peridynamic equations of motion to assess material response. The bricks are equivalent to nodes in Peridynamics, and each brick is now bonded to every other brick within a pre-defined neighbourhood. To explore the impact of how neighbourhoods are defined we consider two neighbourhood types, and a range of sizes. The neighbourhood can be defined by its radius and its type, either a Moore (M) neighbourhood (Figure 4a), which includes bricks that are either orthogonally or diagonally adjacent to the centre brick, or a von Neumann (VN) neighbourhood (Figure 4b), which includes only orthogonally adjacent bricks [45]. In agent-based modelling, generally von Neumann neighbourhoods are used when diagonal interactions are not important to the overall behaviour and Moore neighbourhoods are used when diagonal interactions are required to effectively simulate the macro-scale behaviour. The neighbourhood radius dictates the length scale of material element interactions, the effect of short (R=1) to long (R=5) range, within the microstructural length scale, differences in the strain gradient on the simulated wear rates are evaluated. Moore neighbourhoods of a given radius (R) include twice as many bricks as an equivalent von Neumann neighbourhood of the same radius. This translates to a brick at the centre of a Moore type neighbourhood having twice as many bonds to the material surrounding it as if it had an equivalent von

Neumann type neighbourhood. These factors together determine how well supported by surrounding material each brick is, enabling a wide range of wear mechanisms to be represented.

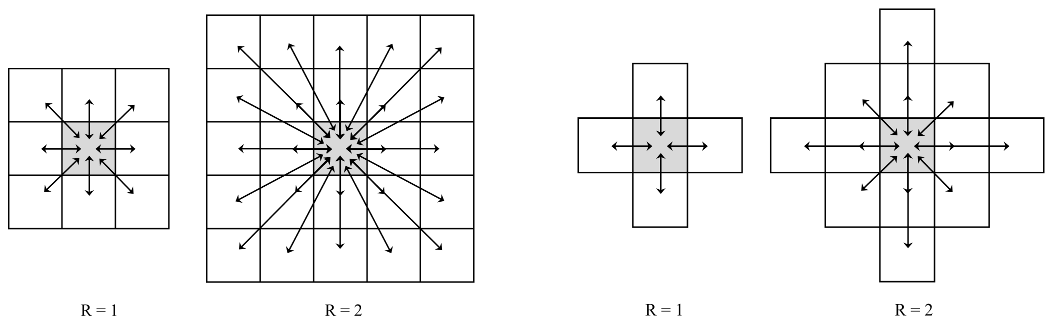

(a) Moore Neighbourhood of Bricks

(b) von Neumann Neighbourhood of Bricks

Figure 4: Neighbourhood types used in the implementation of peridynamic-inspired bonds

The bond failure condition is defined in Equation 4 and as follows. If the magnitude of the difference in strain between two bonded bricks, with indices i,j,k and $i^{'}$,$j^{'}$,$k^{'}$ respectively, is greater than a proportion of the average critical failure strain of the two (γ_{crit}), the bond will fail. The strength of the bonds is a measure of how much residual stress can develop in an effort to maintain strain compatibility in the material before failure. Figure 5 illustrates the conditions of bond failure in a bond between two adjacent bricks; the bond failure constant (BF) controls the strength of the bonds between bricks. The bond failure constant defines the threshold of strain difference that the material can resist before a void or crack forms. On an atomic level, this could be fully defined using molecular dynamics simulations but scaling issues would limit the applicability of any such model. The bond failure constant is therefore defined as material constant, taken to be a percentage of the material's threshold for ductility exhaustion. This can be calibrated against wear rates derived from experimental observation, for example in laboratory twin disc tests, or in material removed from service rails. Bricks do not need to be immediately adjacent to be connected by a bond. In a neighbourhood with radius greater than one, bricks included in that neighbourhood will be bonded in the same fashion as if they were adjacent with the same failure mechanism. Bonds are unaffected by the proximity of the bricks they act between [27] [28].

$$|\gamma^{ijk} - \gamma^{i'j'k'}| \geq \frac{\frac{1}{2}\left(\gamma_{crit}^{ijk} + \gamma_{crit}^{i'j'k'}\right)}{BF} \tag{4}$$

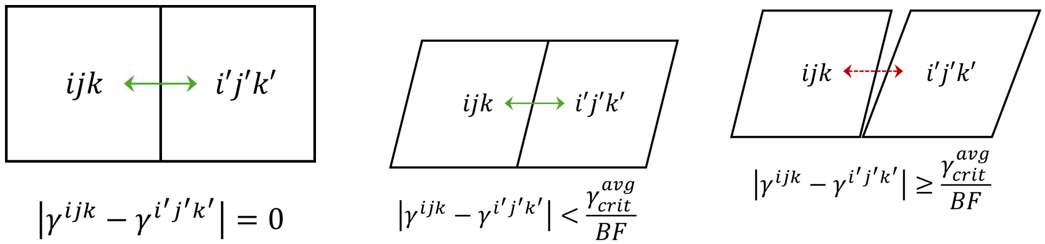

(a) No Strain, Unbroken Bond

(b) Similar Strain, Unbroken Bond

(c) Dissimilar Strain, Broken Bond

Figure 5: Peridynamic-inspired bond failure behaviour between two bonded bricks

The bonds allow the representation of the previously neglected strain incompatibility between adjacent bricks and the stability of the region which will determine whether material is constrained and supported by surrounding less damaged material, or free to leave the surface as wear debris. This overcomes the deficiencies identified above in previous iterations [33] [46]. Figure 6 shows the additional wear mechanism in which a brick at the surface which has no surviving bonds will be removed [47]. , material elements located below the surface are effectively trapped by the surrounding material and cannot be removed as wear debris. Instead, like in the original iterations of the Dynarat model, subsurface material elements with no surviving bonds are unable to resist the residual stresses generated in an attempt to resist differences in strain accumulation response and therefore may be considered a void or point of crack initiation and several in close proximity can be used to represent a microcrack.

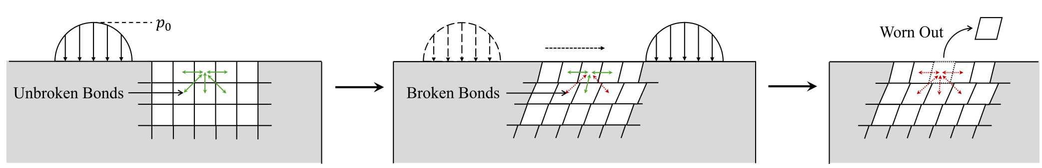

Figure 6: Peridynamic-inspired bonds mechanism for brick removal representing wear [47]

2.2. Competitive Failure Mechanisms

Peridynamics itself has many different failure criteria [30], but the strain-based framework of the Dynarat technique and the previous neglect of a strain incompatibility condition lends itself well to a strain difference failure mechanism. A statistically distributed initial shear yield stress which is used to represent the real variation in properties of a material, for example found through an array of hardness indents [43] means that a strain difference will develop between bricks. This is especially the case at low numbers of contact stress cycles prior to convergence of strains towards the ductility exhaustion limit. Even when subject to identical stress, and it will be greatest in the initial cycles before the bricks harden to a similar effective shear yield stress. To maintain continuity with previous applications of the Dynarat technique, a brick that has reached its critical strain and has exhausted its ductility, is considered failed material. A brick that has failed by ductility exhaustion is subject to the same wear mechanism as one subject to bond breakage alone, and if it is located at the contact surface the same rules will determine when it wears off. This results in a competitive failure process. Wear in the initial cycles, during which strain incompatibility between bricks is at its greatest but accumulated strain is low, is dominated by bond failure and represents the mild wear regime. This improves on previous modelling by representing experimentally observed wear losses at low contact cycle numbers when ratchetting strain accumulation has not yet reached ductility exhaustion before it enters the steady state and possibly a severe wear regime. In later cycles where bricks have accumulated more strain and hardened, such that they reach a similar strain state, wear is dominated by ductility exhaustion.

This competition between failure mechanisms is influenced by material properties and their distribution, providing a route by which the effect on wear and crack initiation of real microstructures can be modelled. This requires the assembly of an appropriate array of bricks with properties representing ferrite or pearlite and will be tackled in future research after the underlying behaviour of the bonded brick technique in representing wear is understood.

3. Results

Simulations were conducted for a range of contact conditions characteristic of rail-wheel contact simulated in a laboratory under twin disc test conditions. The contact conditions simulated are that of a twin disc test, a line contact, with varying maximum Hertzian contact pressure (900MPa, 1200MPa and 1500MPa) and 1% slip [48].The experimental wear rates were acquired through twin disc testing and are published elsewhere [1] [34]. The wear tests were performed using the second Sheffield University ROlling Sliding twin disc machine (SUROS2), Figure 7 a modified Phoenix Tribology TE72 twin disc machine [48]. The test duration for all contact conditions was 70,000 contact cycles, during which the test was interrupted every 10,000 cycles to measure the mass lost from the rail disc. After the conclusion of a test, the discs were sectioned, ground, polished and etched to examine and measure the accumulated strain in the near surface deformed microstructure of the circumferential plane found in the middle of the track width. The angle of the deformed microstructure, θ, is measured and the accumulated strain, γ,can be derived from the relationship described in Equation 5. The experimental procedure described here is a standard method for the characterisation of rail material response to repeated rolling-sliding contact and is described further in [1][49].

$$\gamma = \tan(\theta) \tag{5}$$

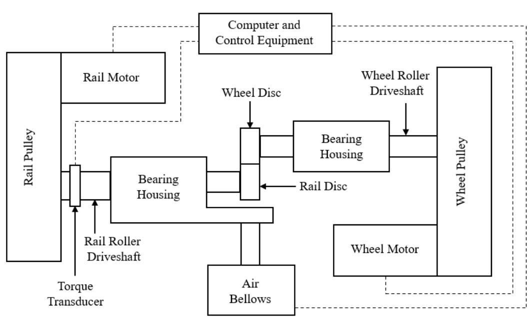

(a) Schematic drawing of the SUROS2 twin-disc machine

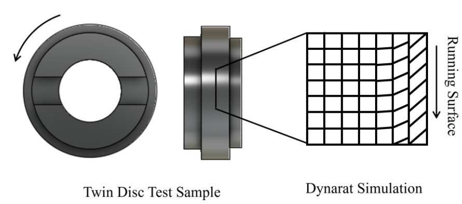

(b) Schematic diagram of the circumferential plane of interest for strain measurements and simulations

Figure 7: Experimental methodology schematic diagrams

The simulated material, for all simulations reported here, consists of a 5mm wide, 2mm deep 2D slice of R260 rail steel which has been discretised into 5µm wide 1µm deep bricks. The maximum orthogonal shear stress distribution varies only in the vertical direction, the brick vertical thickness (1μm) was selected in order prevent inaccuracies by effectively representing the stress distribution and resultant strain gradient. The appropriate vertical thickness was determined from a previous convergence study, that used the original Dynarat technique, including the effect of roughness, which shows that the wear rate becomes insensitive to the effect of vertical thickness with thicknesses $\leq 1.0\mu$m [34]. The brick width is less significant, as the stress distribution does not vary in the longitudinal direction but should be kept small relative to the section size to prevent loss of detail. Assuming that the simulated material represents a small section of a twin disc sample, the behaviour of the simulated material section can be extrapolated across the surface of an entire disc. Therefore, the simulated wear rates have been scaled to represent loss from a full disc (148mm circumference for a 47mm diameter sample of width 10mm). The shear yield stress of each brick was statistically distributed using a mean value (292MPa) and a standard deviation (20MPa) [33] [1]. For all the simulated conditions, the same material constants are used to define the ratchetting and strain accumulation behaviour (Equations 1 and 2). The traction coefficient was measured whilst obtaining the experimental wear rates, which are described elsewhere [34] [1], and is taken here, unless otherwise specified, as 0.4. This reflects the upper bound of the window of coefficient of tractions, experienced after the initial running in period of a twin disc test. A simplified representation of rough surface contact is defined by multiple Hertzian contacts between asperities of the rail surface [50] [51]. By assuming a sinusoidal roughness profile with constant asperity radius and separation, the maximum contact pressure and contact half-width of each asperity contact is determined using the method outlined by Nowell and Hills [52] [38]. The asperity radii and separation, 20μm and 35μm respectively, are determined from the measurement of the surface of twin disc samples, prior to and during a test [34].

3.1. Sensitivity study on bond behaviour

Modelling was undertaken to investigate the effect of neighbourhood type, neighbourhood size (radius) and the bond failure constant (Equation 4) on wear rates predicted using the Peridynamic bond-based failure mechanism in conjunction with the strain exhaustion mechanism. First, the effect of bond failure constant (BF) is considered, which controls whether the bond will fail or not based on the magnitude of strain difference between two bonded bricks. This is shown in Figure 8. A higher bond failure constant means a lower strain difference is required for a bond to fail, whilst a lower value requires a higher strain difference to fail. Figures 8a and 8c which present

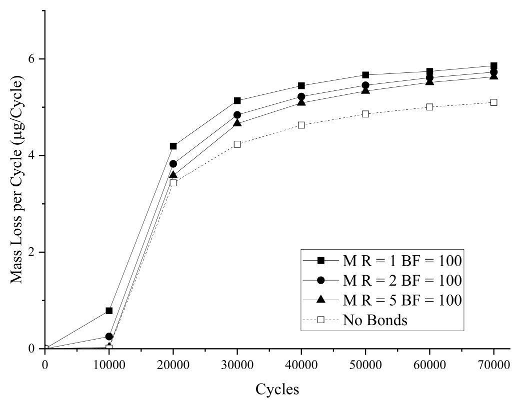

(a) Moore, BF = 100 for R = 1,2 and 5

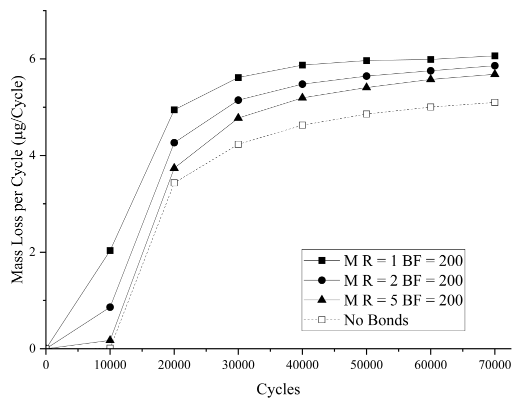

(b) Moore, BF = 200 for R = 1,2 and 5

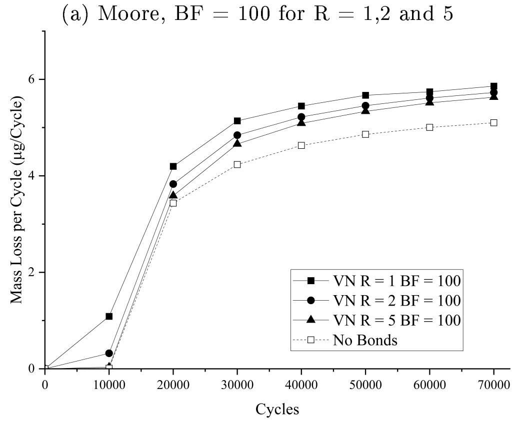

(c) von Neumann, BF = 100 for R = 1,2 and 5

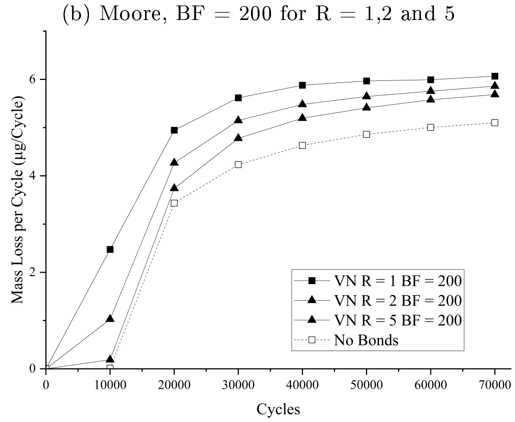

(d) von Neumann, BF = 200 for R = 1,2 and 5

Figure 8: Comparison of effect of different bond failure constants on simulated wear rates of R260 rail steel under repeated rolling sliding contact. 900MPa maximum contact pressure and 1% slip

the wear rates of Moore and von Neumann neighbourhoods with $BF = 100$, have lower wear rates than their respective equivalents, Figures 8b and 8d with $BF = 200$. As would be expected, a larger bond failure constant produces higher wear rates, as it lowers the strain difference needed to break a brick's bonds with its neighbours, enabling it to wear off. This is true for both neighbourhood types and across neighbourhood radii $R = 1$, $R = 2$ and $R = 5$. The most notable outcome of the introduction of the new mechanism and the various parameters that define it, is the effect it has on the wear behaviour in the first 10,000 cycles. The introduction of bonds has allowed for the representation and control of wear rates in the early stages of the simulation, which is not possible if ratchetting strain exhaustion alone is considered. Varying the bond failure constant has a significant influence over the rate of wear, but its impact varies between neighbourhoods of different radii. In Figure 8, for both Moore and von Neumann neighbourhoods, the larger radii simulations have lower wear rates regardless of the bond failure constant. Larger radii neighbourhoods contain more bricks and therefore more bonds must be broken for a brick to leave the surface as a result of the strain difference failure mechanism. The bond failure constant can be normalised between two simulations of different radii by multiplying the bond failure constant by the ratio of their radii. This, as illustrated in Figure 9, means that they will produce almost identical wear rates, for both Moore and von Neumann neighbourhoods. This indicates that neighbourhood radius has minimal effect on wear rates when the radius of the neighbourhood is accounted for in the bond failure criteria. When the results of simulations with Moore or von Neumann neighbourhoods are plotted on the same axis, as shown in Figure 10, the negligible influence the choice of neighbourhoods has have on the wear rates becomes apparent. Despite the fact that Moore neighbourhoods contain more bricks, and therefore bonds, than a von Neumann neighbourhood at larger radii the wear rates remain consistent between them. At smaller radii Figure 10a shows that von Neumann neighbourhoods produce slightly higher wear rates in the initial 10k cycles than Moore neighbourhoods. This can be explained by the shape of the respective neighbourhoods, illustrated in Figure 3. Whilst Moore neighbourhoods contain more bricks than a von Neumann neighbourhood, the location of these additional bricks provide insight into why they behave so similarly. The additional bricks are located in the layers above and below the reference brick (shown in grey in Figure 3), meaning that the stress they will experience will be different to the central reference brick. In a rough contact, the maximum orthogonal shear stress will vary rapidly with depth at the near surface. For the asperity tip radii and spacing investigated this variation can be up to 250MPa in 1μm under a bulk contact pressure of 900MPa. This is much greater than any statistical variation in shear yield strength between bricks in different layers. This means that the variation in the stress distribution is the primary controlling factor for any variation in strain between bricks in different layers. Therefore, despite a Moore neighbourhood having more bricks below or above the central reference brick, their respective bonds will all fail nearly simultaneously, effectively behaving as one brick as if it were a von Neumann neighbourhood. The results show that the most important factor in controlling the wear as a result of the strain difference failure mechanism is the bond failure constant. The effect of changing the radius can be accounted for by normalising the bond failure constant using the radius and for a rough surface stress distribution the difference between the behaviour of a Moore and von Neumann neighbourhood is negligible. However, it is worth noting that, in reality, the bond failure constant, neighbourhood type and size represent a combination for which model will be calibrated against experiments. There is limited purpose in varying these factors individually.

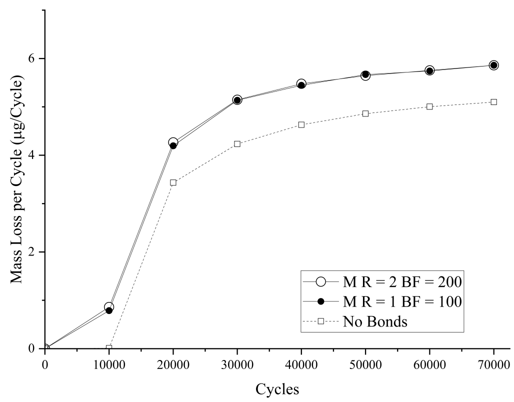

(a) Moore, Normalised BF for R = 1 and 2

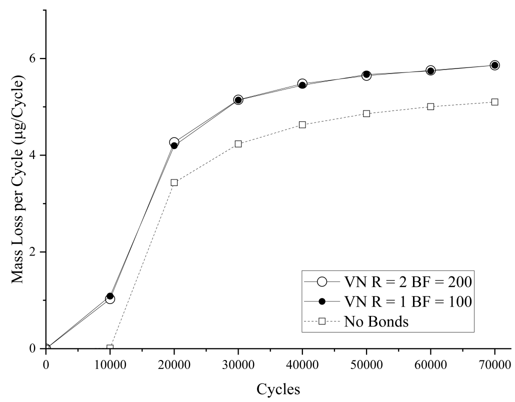

(b) von Neumann, Normalised BF for R = 1 and 2

Figure 9: Comparison of effect of different neighbourhood radii with normalised bond failure constants on simulated mass loss of R260 rail steel under repeated rolling sliding contact. 900MPa maximum contact pressure and 1% slip

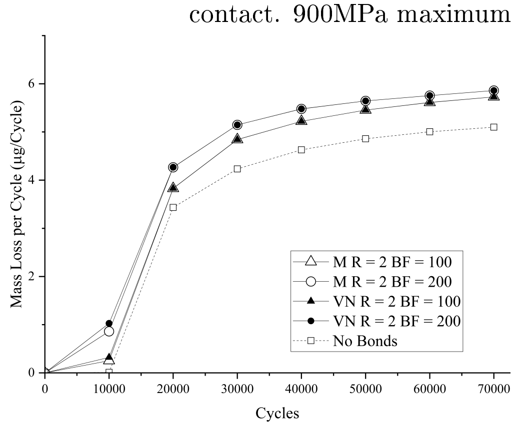

(a) Moore vs von Neumann, R = 2 BF = 100, 200

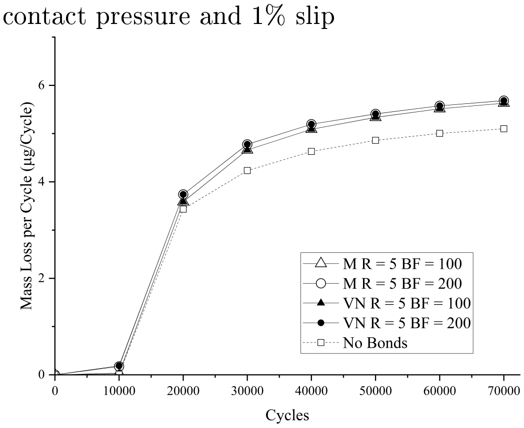

(b) Moore vs von Neumann, R = 5 BF = 100, 200

Figure 10: Comparison of effect of different neighbourhood types on simulated mass loss of R260 rail steel under repeated rolling sliding contact. 900MPa maximum contact pressure and 1% slip

3.2. Validation of wear rate

Two datasets were used to explore the model containing both strain exhaustion and strain difference failure mechanisms: (i) calibration, and (ii) validation. First the bond parameters were tuned producing the data in Figure 11. This illustrates the capability of the strain difference failure mechanism, when tuned appropriately, to bring the wear rates of the simulated material in the first 10,000 cycles into much closer agreement to those observed experimentally, increasing the wear rates in the first 10,000 cycles by 2.4μg/cycles, whilst being able to maintain the steady state behaviour through the strain exhaustion mechanism. This calibration stage is the equivalent of determining the wear coefficient in the Archard wear law [53]. The failure mechanism

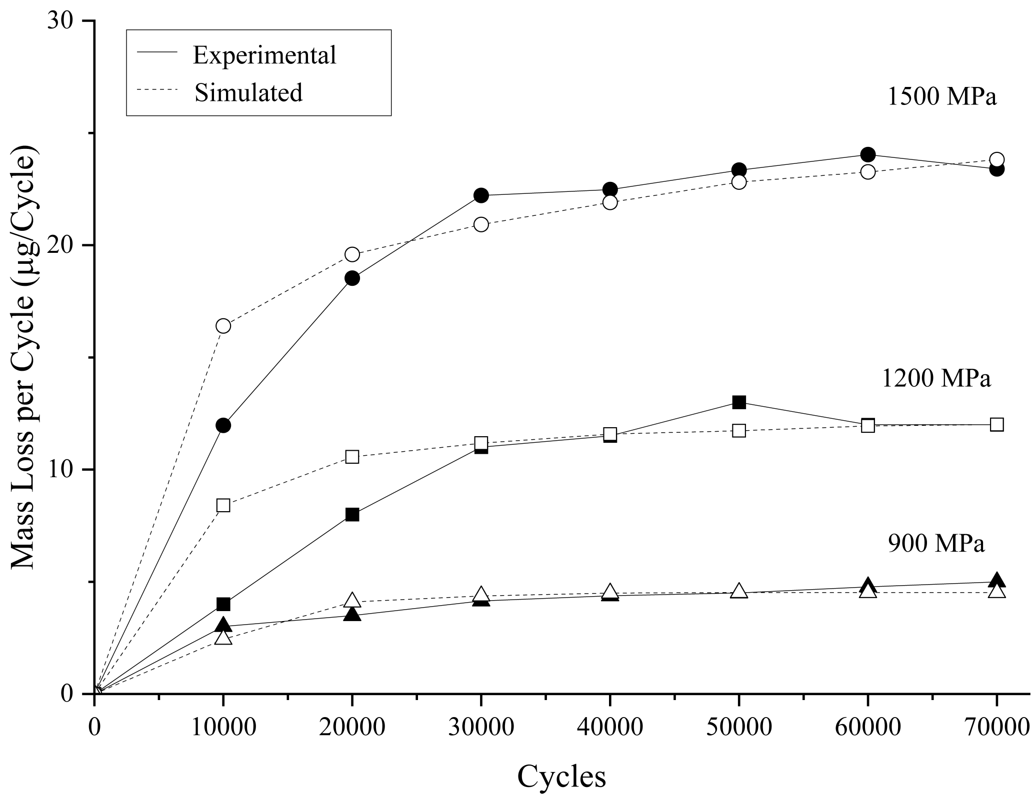

Figure 11: Simulated wear rates of R260 rail steel compared with experimentally determined wear rates under repeated rolling sliding contact with the addition of a strain difference failure mechanism. Neighbourhood Type = von Neumann, Neighbourhood Radius = 1 and BF Constant = 150

has only been calibrated against the 900MPa contact condition and subsequently applied to 1200MPa and 1500MPa cases and has only had minor effects on the material response, raising the wear rates in the initial cycles by a comparable amount (2.6μg/cycles and 2.2μg/cycles respectively) in the first 10,000 cycles. This is consistent with the influence of a strain difference failure mechanism, which is most prominent in the initial cycles. The bond failure constant is assumed to be a material property, consistent across loading conditions. Here the bond failure constant has been tuned against the 900MPa case and directly applied to the 1200MPa and 1500MPa cases. Future calibration should incorporate the 1500MPa and 1200MPa cases to ensure universality of the constant.

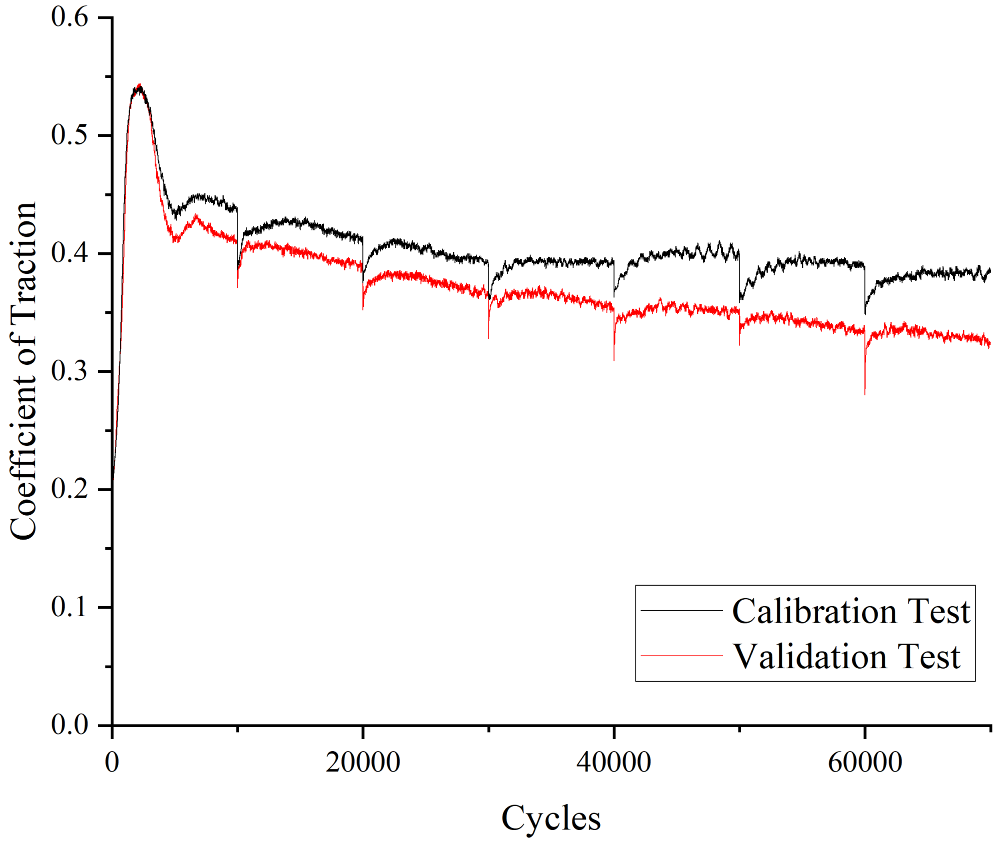

Figure 12: Coefficient of Traction measured during twin disc testing to obtain wear rates for calibration and validation of simulated wear rates

To validate the tuned behaviour, a separate series of twin disc experiments was performed to obtain wear rates independent of those used for tuning. Figure 12 shows the coefficient of traction for both the tuning and calibration wear tests.There exists a spread of results, in terms of wear rates and coefficient of tractions, from twin disc tests conducted under nominally identical test conditions [34, 1, 54]. This arises from differences in humidity and temperature on the days the tests are conducted, which can have a significant impact on oxide formation of the surface of the discs. Given these inevitable differences between tests, in order to validate the model, a second simulation was run with a friction coefficient that reflects the lower bound (0.35) of the window of traction coefficients observed experimentally. This is used to explore the ability of the model to respond to changes in sur-

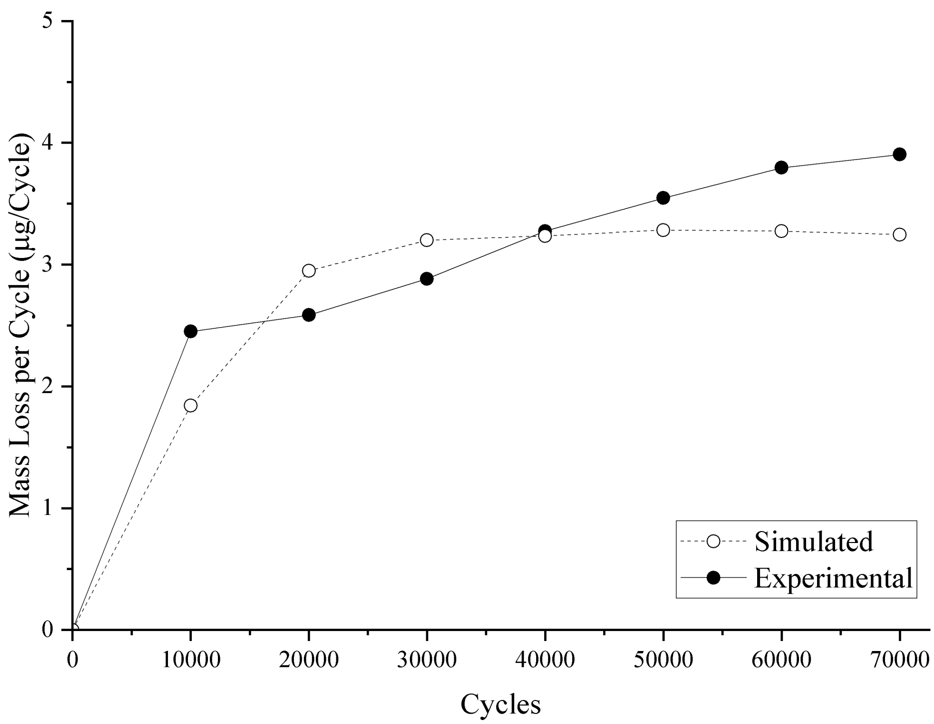

Figure 13: Validation of simulated wear rates of R260 rail steel including the Peridynamic strain difference failure mechanism compared with independent experimentally determined wear rates under 900MPa bulk contact pressure, 1% slip. Neighbourhood Type = von Neumann, Neighbourhood Radius = 1 and BF Constant = 150

face friction behaviour. Figure 13 shows the results of the tuned simulation for the lower bound friction case, compared with experimentally determined wear rates of the same contact conditions. The experimental results presented in Figure 13 are independent of the tuning process and are used to validate the simulated material response. The simulation shows good correlation to experimental behaviour, with a root mean squared error (RSME) of 0.42μg/Cycle between the simulated and experimental wear rates. The behaviour also exhibits a similar drop in the wear rate as a result of the lower coefficient of friction. This strongly supports the modelling technique and the new failure mechanism, showing that the model is successful in predicting experimental outcomes outside the data it has been tuned against.

3.3. Validation of subsurface strain accumulation

Predicted wear rates are dependent not only on near surface behaviour, including that represented by the newly introduced bonds, but also subsurface strain accumulation prior to exposure at the surface as wear takes place. In addition to validating surface wear rates, sub-surface behaviour has been validated against experimental strain measurements not used in defining the governing equations. The ratchetting process represented in the new GPU accelerated model had already been verified against previous publications using BS11 steel [55, 33, 38]. In this paper, however, the behaviour of simulated R260 rail steel is considered. Figure 14 shows the simulated accumulation of strain in the material with depth after 15k cycles and 40k cycles, compared with experimental strain measurements taken after twin disc tests of the same conditions and duration [34, 1]. The scatter points of simulated results have been downsampled for visual clarity. The fitted relationship from which the root mean square error (RMSE) is calculated however is derived from full dataset. The simulations used to generate these results included wear driven by both bond failure and strain exhaustion mechanisms, tuned as for Figure 11. Excellent agreement is seen between experimental and simulated sub-surface strain; however, there was some discrepancy within 100μm of the surface, where the effects of rough surfaces and asperity contact have the most influence, this also being the region in which experimental strain measurement is extremely challenging as the microstructure becomes so deformed it is difficult to resolve [55]. The error between the simulated and experimental results is low, 0.830-0.897, indicating that the simulated sub-surface behaviour and the loading history of a brick as it approaches the surface are representative of experimental behaviour. Moreover, it confirms that the introduction of the novel bond breakage failure mechanism has not affected strain accumulation in the deeper material for which strain accumulation is the dominant degradation process.

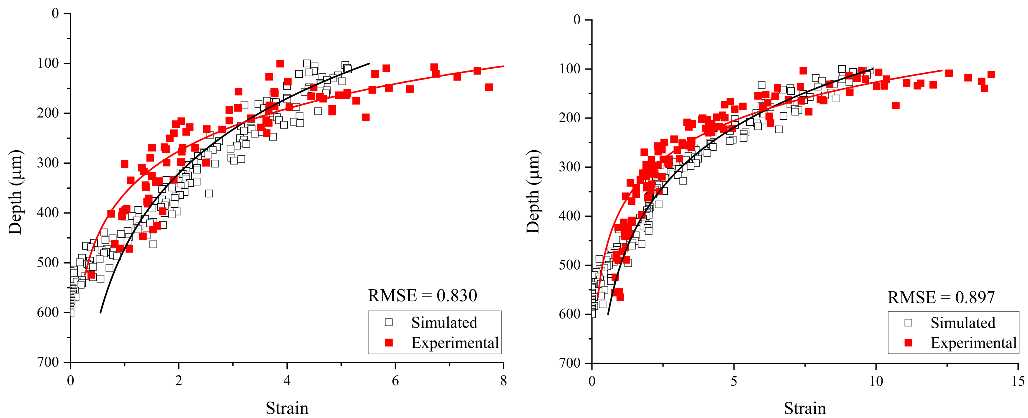

(a) 15,000 Cycles

(b) 40,000 Cycles

Figure 14: Strain Accumulation with depth of simulated material subject to 1500MPa bulk contact pressure 1% slip compared with experimental material subject to the same conditions. Scatter of simulated results have been downsampled for visual clarity.

4. Discussion

Peridynamic-inspired bonds have facilitated the introduction of a new brick removal mechanism that acts with the established strain exhaustion mechanism. It has been shown that, through tuning of the bond parameters, the new mechanism can influence the initial simulated wear rates, which at low contact pressures, where the strain increment per cycle during ratchetting is small and ductility exhaustion is reached much later in the simulation, are a result of mild wear, whilst maintaining the steady state behaviour. This has been validated against experimental results, including the transition between these regimes produced under the lower bound of the window of coefficient of tractions experienced during a twin disc test. Whilst severe contact conditions that are known to induce ratchetting (1500MPa, 1200MPa, 900MPa 1% slip) have been explored, the demonstrated ability of the new mechanism to represent material removal in the mild wear regime is an important addition. It offers the opportunity for the simulation of less severe contact conditions which could not be represented by a ratchetting and ductility exhaustion-based model alone. These may exist in steady state under less severe contact conditions, or as illustrated in the tests reported here form a transient period as new material accumulates strain under severe conditions. The simulated wear rates depend mostly on the chosen bond failure constant, in conjunction with the chosen neighbourhood radius, whilst neighbourhood type has little to no influence.

Although inclusion of the additional failure mechanism brings the simulated wear rates into closer agreement with experimental observations there are still some areas in which refinement is possible, such as in high stress gradients where variation in stress between layers of bricks exceeds the variation in shear yield stress and renders the effect of different neighbourhood types negligible on the wear rates. In addition, the model presented in this paper lacks the ability to represent the strain localisation and partitioning observed in real steels [5], due to properties of the rail section being distributed statistically instead of representing their true spatial distribution across a microstructure.

Microstructures have been introduced in previous iterations of the brick model, using bricks of varying material properties to represent the ferrite and pearlite constituents [42], although at that time the model had no way to consider strain partitioning between the bricks. The bonds between bricks, and the accompanying strain difference failure mechanism offer the potential to represent the strain partitioning between ferrite and pearlite and resulting crack initiation behaviour. The primary limitation of the statistical representation of the material properties is that the model cannot represent larger scale regions of de-cohesion that represent preferential void formation and crack initiation along grain boundaries containing proeutectoid ferrite, an effect that has been documented experimentally at both nano and macro-scales in ferritic pearlitic steels [1][2]. Therefore, the model, and any simulation outputs, cannot consider experimental behaviour that arises from microstructural effects such as flaking of the surface, development of surface breaking cracks and the development of a surface roughness as a result. For R260 there is unlikely to be a significant change in wear rates with the introduction of microstructurally distributed properties due to the limited amount of proeutectoid ferrite present in the steel and the fact that neighbourhood radii considered are within the microstructural length scale [43]. For finer microstructure, premium grade steels where there is little to no proeutectoid ferrite or any heterogeneity in the microstructure cannot be resolved, a statistical microstructure is sufficiently descriptive to represent the wear behaviour. However, simulations of BS11, R200 or R220 grade steels which have a significant proportion of proeutectoid ferrite would likely fail to adequately represent wear behaviour that is dominated by the strain difference mechanism and material de-cohesion and would. Similarly, the significant role grain boundary proeutectoid ferrite has in crack initiation and surface damage could not be represented. Strain localisation as a result of differences in material properties distributed across a microstructure may also account for deviations between simulated and experimentally observed strain accumulation.

The simplified representation of roughness as a sinusoidal surface with equally spaced asperities with equal radii is a further area in which the model could be refined, although this is effectively an input condition for the model rather than a core aspect of the strain or failure modelling. For example. a real contact will experience asperities of different separations and radii which will change over the duration of a twin disc test whereas a uniform roughness has been assumed in the current work. The effect of different asperity radii and separations on the simulated material is the subject of ongoing research elsewhere and is an important next step in the validation of the model. The application of this model to full scale, three-dimensional rail-wheel contact is of significant importance if infrastructure managers are to use it to predict rail failure. While three dimensional contacts can and have been previously implemented with the Dynarat technique but can only consider strain in the longitudinal direction and have a higher computation time due to the more intensive stress calculations required [38]. Although it is common for laboratory scale twin disc wear behaviour to be related and compared to full-scale behaviour using contact patch area, most of the understanding of ratchetting strain accumulation has been developed for twin disc two-dimensional contacts [53]. It is possible, when moving to three-dimensional full-scale contacts the ratchetting laws will change, especially with the introduction of lateral or spin creepages. However, the model has demonstrated good agreement with laboratory scale two-dimensional contacts and the latter discussion point forms the basis of a larger body of work for the model development. Finally, just as the peridynamic style bonds have facilitated the strain incompatibility mechanism which in this paper has been used to simulate wear in the mild regime, they may also facilitate modelling additional aspects of rail steel response to loading. For example, pearlite mechanical properties are affected by the strain rate [56][57] and bond behaviour may be a route to represent this for the investigation of impact loading.

5. Conclusions

A new model has been developed extending the previous "Dynarat" model in two key aspects: (i) successful re-implementation using the FLAME-GPU framework to enable rapid computation, and (ii) representation of an additional material failure mechanism crucial to prediction of early-stage mild wear prior to strain exhaustion. The established strain exhaustion mechanism, when combined with a simulated rough contact, can be used to replicate steady state experimental wear rates of a twin disc test. However, at low contact pressures the strain exhaustion mechanism alone cannot represent the initial material removal observed experimentally which is in the mild wear regime. A strain difference failure mechanism, in the form of peridynamic bonds, has been shown to be capable of addressing this and can act in conjunction with the strain exhaustion mechanism, maintaining steady state behaviour in the severe wear regime. The strain difference failure mechanism can be calibrated against experimental behaviour to determine the most appropriate material bond parameters. Calibration is most dependent on the bond failure constant. The effect of neighbourhood radius can be normalised by adjusting the bond failure constant and neighbourhood type has a negligible effect on wear rates. When calibrated, the simulated wear rates have been validated against independent wear data under different contact conditions, retaining good correlation with an RMSE of 0.42. The new mechanism presents a number of opportunities for the modelling of rail failure. Less severe contact conditions where ratchetting does not occur could now be simulated, including transition to higher wear rates for cases that promote ratchetting failure over many contact cycles such as in harder, premium grade rail steels. Moreover, with properties distributed over a microstructure, the new mechanism has the potential to represent material failure as a result of strain localisation in microstructural constituents.

CRediT authorship contribution statement

Philomenah Holladay: Conceptualization, Visualization, Writing - original draft, Writing - review & editing, Software, Visualization, Investigation, **Mark Burstow:** Supervision, Conceptualization, Writing - review

& editing, **Francis Franklin:** Conceptualization, Writing - review & editing, Methodology, **Adam Wilby:** Investigation, Validation, Writing - review & editing, **David Fletcher:** Conceptualization, Supervision, Software, Methodology, Writing - review & editing, Funding acquisition

Declaration of Competing Interest

The authors declare that they have no known competing financial interests or personal relationships that could have appeared to influence the work reported in this paper.

Acknowledgements

The author wishes to acknowledge the funding received for this research from Network Rail, The University of Sheffield, EPSRC and SFI Centre for Doctoral Training in Advanced Metallic Systems (EP/S5022635/1).

References

[1] A. Wilby, J. Corteen, S. Lewis, R. Lewis, D. I. Fletcher, Nano and micro-indentation driven characterisation of asperity and bulk plasticity at the surface of modern premium rail steels, Wear 530-531 (2023). doi:10.1016/j.wear.2023.205004.

[2] A. Kapoor, A re-evaluation of the life to rupture of ductile metals by cyclic plastic strain, Fatigue and Fracture of Engineering Materials and Structures 17 (2) (1994) 201–219. doi:10.1111/j.1460-2695.1994.tb00801.x.

[3] N. P. Suh, The delamination theory of wear, Wear 25 (1973) 111–124.

[4] J. Zhang, A. T. Alpas, Delamination wear in ductile materials containing second phase particles, Materials Science and Engineering A160 (1992) 25–35.

[5] J. E. Garnham, C. L. Davis, Very early stage rolling contact fatigue crack growth in pearlitic rail steels, Wear 271 (1-2) (2011) 100–112. doi:10.1016/j.wear.2010.10.004.

[6] D. I. Fletcher, J. Beynon, Equilibrium of crack growth and wear rates during unlubricated rolling-sliding contact of pearlitic rail steel, Proceedings of the Institution of Mechanical Engineers, Part F: Journal of Rail and Rapid Transit 214 (2) (2000) 93–105.

[7] Office of Rail and Road (ORR), Annual efficiency and finance assessment of network rail 2024, Report (2024).

[8] M. Burstow, Whole life rail model application and development: Development of a rolling contact fatigue damage parameter (burstow report), Report, Rail Safety and Standard Board (RSSB) (2003).

[9] Network Rail, Control period 7 (cp7) variable usage charge (vuc), process and policy for the proposal and consent of new rates., Report (2024).

[10] P. J. Rogers, Investigation into the effects of reducing primary yaw stiffness on rolling contact fatigue generation, Report, Rail Safety and Standards Board (RSSB) (2008).

[11] P. Clayton, The relations between wear behaviour and basic material properties for pearlitic steels, Wear 60 (1980) 75–93.

[12] U. Olofsson, T. Telliskivi, Wear, plastic deformation and friction of two rail steels - a full-scale test and a laboratory study, Wear 254 (2003) 80–93.

[13] M. Burstow, Experience of premium grade rail steels to resist rolling contact fatigue (rcf) on gb network, Ironmaking and Steelmaking 40 (2) (2013) 103–107. doi:10.1179/1743281212y.0000000042.

[14] F. Ren, Z. Yang, Z. Li, An efficient 3d finite element procedure for simulating wheel–rail cyclic contact and ratcheting, Tribology International 198 (2024). doi:10.1016/j.triboint.2024.109878.

[15] H. Su, C. L. Pun, P. Mutton, Q. Kan, W. Yan, Numerical study on the ratcheting performance of heavy haul rails in curved tracks, Wear 436-437 (2019). doi:10.1016/j.wear.2019.203026.

[16] C. L. Pun, Q. Kan, P. J. Mutton, G. Kang, W. Yan, An efficient computational approach to evaluate the ratcheting performance of rail steels under cyclic rolling contact in service, International Journal of Mechanical Sciences 101-102 (2015) 214–226. doi:10.1016/j.ijmecsci.2015.08.008.

[17] W. Daves, W. Kubin, S. Scheriau, M. Pletz, A finite element model to simulate the physical mechanisms of wear and crack initiation in wheel/rail contact, Wear 366-367 (2016) 78–83. doi:10.1016/j.wear.2016.05.027.

[18] Y. Li, Y. Wu, P. Mutton, C. Qiu, W. Yan, A ratcheting mechanism-based numerical model to predict damage initiation in twin-disc tests of premium rail steels, Engineering Failure Analysis 146 (2023). doi:10.1016/j.engfailanal.2023.107066.

[19] Q. Lian, G. Deng, A. K. Tieu, H. Li, Z. Liu, X. Wang, H. Zhu, Thermo-mechanical coupled finite element analysis of rolling contact fatigue and wear properties of a rail steel under different slip ratios, Tribology International 141 (2020). doi:10.1016/j.triboint.2019.105943.

[20] M. Pletz, W. Daves, W. Yao, W. Kubin, S. Scheriau, Multi-scale finite element modeling to describe rolling contact fatigue in

a wheel–rail test rig, Tribology International 80 (2014) 147–155. doi:10.1016/j.triboint.2014.07.005.

[21] P.-R. Cha, D. J. Srolovitz, T. Kyle Vanderlick, Molecular dynamics simulation of single asperity contact, Acta Materialia 52 (13) (2004) 3983–3996. doi:10.1016/j.actamat.2004.05.014.

[22] C. Hong, T. Chen, Z. Li, A. Du, M. Liu, P. Liu, Y. Lu, Uniaxial ratcheting behavior and molecular dynamics simulation evaluation of 316ln stainless steel, Materials Science and Engineering: A 849 (2022). doi:10.1016/j.msea.2022.143535.

[23] K. Wang, J. Lai, J. Xu, T. Liao, P. Wang, R. Chen, Y. Qian, L. Li, X. Ma, Multiscale analysis of wheel-rail rolling contact wear and damage mechanisms using molecular dynamics and explicit finite elements, Tribology International 185 (2023). doi:10.1016/j.triboint.2023.108574.

[24] J. S. Koehler, On the dislocation theory of plastic deformation, Physical Review 60 (5) (1941) 397–410. doi:10.1103/PhysRev.60.397.

[25] A. Freimanis, S. Kaewunruen, Peridynamic analysis of rail squats, Applied Sciences 8 (11) (2018). doi:10.3390/app8112299.

[26] M. Januschewsky, G. Trummer, K. Six, R. Lewis, Discrete element modelling of rolling contact fatigue and crack closure with different bond laws, Wear 544-545 (2024). doi:10.1016/j.wear.2024.205268.

[27] S. A. Silling, M. Epton, O. Weckner, J. Xu, E. Askari, Peridynamic states and constitutive modeling, Journal of Elasticity 88 (2) (2007) 151–184. doi:10.1007/s10659-007-9125-1.

[28] S. A. Silling, E. Askari, A meshfree method based on the peridynamic model of solid mechanics, Computers and Structures 83 (17-18) (2005) 1526–1535. doi:10.1016/j.compstruc.2004.11.026.

[29] D. Dipasquale, G. Sarego, M. Zaccariotto, U. Galvanetto, A discussion on failure criteria for ordinary state-based peridynamics, Engineering Fracture Mechanics 186 (2017) 378–398. doi:10.1016/j.engfracmech.2017.10.011.

[30] E. Madenci, S. Oterkus, Ordinary state-based peridynamics for plastic deformation according to von mises yield criteria with isotropic hardening, Journal of the Mechanics and Physics of Solids 86 (2016) 192–219. doi:10.1016/j.jmps.2015.09.016.

[31] L. Wang, X. Sheng, J. Luo, A peridynamic frictional contact model for contact fatigue crack initiation and propagation, Engineering Fracture Mechanics 264 (2022). doi:10.1016/j.engfracmech.2022.108338.

[32] D. A. Abdoh, B. B. Yin, V. K. R. Kodur, K. M. Liew, Computationally efficient and effective peridynamic model for cracks and fractures in homogeneous and heterogeneous materials, Computer Methods in Applied Mechanics and Engineering 399 (2022). doi:10.1016/j.cma.2022.115318.

[33] F. J. Franklin, I. Widiyarta, A. Kapoor, Computer simulation of wear and rolling contact fatigue, Wear 251 (2001) 949–955.

[34] A. Wilby, Characterisation and understanding of rail steel behaviour for in-service life prediction, Ph.D. thesis, University of Sheffield (2023).

[35] J. E. Garnham, C. L. Davis, The role of deformed rail microstructure on rolling contact fatigue initiation, Wear 265 (9-10) (2008) 1363–1372. doi:10.1016/j.wear.2008.02.042.

[36] T. Vermeij, J. P. M. Hoefnagels, Plasticity, localization, and damage in ferritic-pearlitic steel studied by nanoscale digital image correlation, Scripta Materialia 208 (2022). doi:10.1016/j.scriptamat.2021.114327.

[37] P. Richmond, M. K. Chimeh, Flame gpu: Complex system simulation framework, in: 2017 International Conference on High Performance Computing and Simulation (HPCS), 2017, pp. 11–17. doi:10.1109/hpcs.2017.12.

[38] D. Fletcher, P. Holladay, P. Richmond, Flamegpu agent based modelling for rail-wheel materials, in: 13th International Conference on Contact Mechanics and Wear of Rail/Wheel Systems (CM2025), 2025.

[39] F. J. Franklin, T. Chung, A. Kapoor, Ratcheting and fatigue-led wear in rail–wheel contact, Fatigue and Fracture of Engineering Materials and Structures 26 (10) (2003) 949–955. doi:10.1046/j.1460-2695.2003.00703.x.

[40] F. J. Franklin, A. Kapoor, Modelling wear and crack initiation in rails, Proceedings of the Institution of Mechanical Engineers, Part F: Journal of Rail and Rapid Transit 221 (1) (2007) 23–33. doi:10.1243/0954409jrrt60.

[41] W. R. Tyfour, J. Beynon, A. Kapoor, Deterioration of rolling contact fatigue life of pearlitic rail steel due to dry-wet rolling-sliding line contact, Wear 197 (1996) 255–265.

[42] G. Vasić, F. J. Franklin, D. I. Fletcher, Influence of partial slip and direction of traction on wear rate in wheel-rail contact, Wear 270 (3-4) (2011) 163–171. doi:10.1016/j.wear.2010.10.012.

[43] P. Holladay, M. Burstow, F. Franklin, D. Fletcher, Wear and fatigue of three pearlitic rail steels in a bonded brick model for rail failure, in: 13th International Conference on Contact Mechanics and Wear of Rail/Wheel Systems (CM2025), 2025.

[44] D. I. Fletcher, F. J. Franklin, A. Kapoor, Image analysis to reveal crack development using a computer simulation of wear and rolling contact fatigue, Fatigue and Fracture of Engineering Materials and Structures 26 (10) (2003) 957–967. doi:10.1046/j.1460-2695.2003.00696.x.

[45] J. Kari, Theory of cellular automata: A survey, Theoretical Computer Science 334 (1) (2005) 3–33. doi:https://doi.org/10.1016/j.tcs.2004.11.021.

[46] W. R. Tyfour, J. Beynon, A. Kapoor, The steady state wear behaviour of pearlitic rail steel under dry rolling - sliding contact conditions, Wear 180 (1995) 79–89.

[47] X. Wang, S. Ma, W. Dong, X. Zhao, B. An, Q. He, H. Ding, P. Wang, W. Wang, Peridynamic modeling of rail wear during sliding contact considering thermal effects, Wear 532-533 (2023). doi:10.1016/j.wear.2023.205110.

[48] K. Tomlinson, D. I. Fletcher, R. Lewis, Evaluation of laser cladding as an in-situ repair method on rail steel, Tribology International 180 (2023). doi:10.1016/j.triboint.2022.108210.

[49] K. Tomlinson, D. I. Fletcher, R. Lewis, Measuring material plastic response to cyclic loading in modern rail steels from a minimal number of twin-disc tests, Proceedings of the Institution of Mechanical Engineers, Part F: Journal of Rail and Rapid Transit 235 (10) (2021) 1203–1213. doi:10.1177/0954409721993615.

[50] A. Kapoor, F. J. Franklin, S. K. Wong, M. Ishida, Surface roughness and plastic flow in rail wheel contact, Wear 253 (2002) 257–264.

[51] D. I. Fletcher, J. Corteen, A. Wilby, Rough surface rolling contact fatigue crack stress intensity factor calculation for modern rail steels, Wear 540-541 (2024). doi:10.1016/j.wear.2023.205231.

[52] D. Nowell, D. A. Hills, Hertzian contact of ground surfaces, Journal of Tribology 111 (1989) 175–179.

[53] R. Lewis, U. Olofsson, Mapping rail wear regimes and transitions, Wear 257 (7-8) (2004) 721–729. doi:10.1016/j.wear.2004.03.019.

[54] A. Athukorala, D. V. De Pellegrin, Experimental depiction of the hypothesis of flake-like wear debris generation in rolling contact fatigue of the rail–wheel contact interface, Tribology Transactions 60 (4) (2016) 581–591. doi:10.1080/10402004.2016.1188189.

[55] A. Kapoor, J. H. Beynon, D. I. Fletcher, M. Loo-Morrey, Computer simulation of strain accumulation and hardening for pearlitic rail steel undergoing repeated contact, Journal of Strain Analysis 39 (4) (2004) 383–396.

[56] Z. Li, X. Zhao, C. Esveld, R. Dollevoet, M. Molodova, An investigation into the causes of squats—correlation analysis and numerical modeling, Wear 265 (9-10) (2008) 1349–1355. doi:10.1016/j.wear.2008.02.037.

[57] L.-W. Liang, S.-C. Dai, Y. Chen, H.-Y. Wang, Y.-J. Wang, L.-H. Dai, Emergent failure transition of pearlitic steel at extremely high strain rates, Computational Materials Science 219 (2023). doi:10.1016/j.commatsci.2022.112005.